Specific mechanisms of chromosomal instability indicate therapy sensitivities in high-grade serous ovarian carcinoma.

Naoka Tamura[1†], Nadeem Shaikh[1†], Daniel Muliaditan[1], Tanya N. Soliman[1], Jennifer R. McGuinness[1], Eleni Maniati[1], Daniela Moralli[2], Mary-Anne Durin[2], Catherine M. Green[2], Frances R. Balkwill[1], Jun Wang[1], Kit Curtius[1,3,4], Sarah E. McClelland[1*]

[1]Barts Cancer Institute, Queen Mary University of London, London EC1M 6BQ, UK. [2]Chromosome Dynamics, Wellcome Centre for Human Genetics, University of Oxford, OX3 7BN, UK. [3]Division of Biomedical Informatics, Department of Medicine, University of California San Diego, La Jolla, CA, USA. [4]Moores Cancer Center, University of California San Diego, La Jolla, CA, USA.

*Correspondence to: s.mcclelland@qmul.ac.uk

† Authors contributed equally to the work

The authors declare no potential conflicts of interest.

Running Title: Mechanisms of Chromosomal Instability in Ovarian Cancer

Abstract

Chromosomal instability (CIN) comprises continual gain and loss of chromosomes or parts of chromosomes and occurs in the majority of cancers, often conferring poor prognosis. Due to a scarcity of functional studies and poor understanding of how genetic or gene expression landscapes connect to specific CIN mechanisms, causes of CIN in most cancer types remain unknown. High-grade serous ovarian carcinoma (HGSC), the most common subtype of ovarian cancer, is the major cause of death due to gynaecological malignancy in the Western world, with chemotherapy resistance developing in almost all patients. HGSC exhibits high rates of chromosomal aberrations and knowledge of causative mechanisms would represent an important step towards combating this disease. Here we perform the first in-depth functional characterization of mechanisms driving CIN in HGSC in seven cell lines that accurately recapitulate HGSC genetics. Multiple mechanisms co-existed to drive CIN in HGSC, including elevated microtubule dynamics and DNA replication stress that can be partially rescued to reduce CIN by low doses of paclitaxel and nucleoside supplementation, respectively. Distinct CIN mechanisms indicated relationships with HGSC-relevant therapy including Poly (ADP-Ribose) Polymerase (PARP) inhibition and microtubule-targeting agents. Comprehensive

genomic and transcriptomic profiling revealed deregulation of various genes involved in genome stability but were not directly predictive of specific CIN mechanisms, underscoring the importance of functional characterization to identify causes of CIN. Overall, we show that HGSC CIN is complex and suggest that specific CIN mechanisms could be used as functional biomarkers to indicate appropriate therapy.

Statement of Significance

Findings characterize multiple deregulated mechanisms of genome stability that lead to chromosomal instability in ovarian cancer and demonstrate the benefit of integrating analysis of said mechanisms into predictions of therapy response.

Introduction

The vast majority of solid tumours exhibit chromosomal instability (CIN), the continual gain and loss of chromosomes or parts of chromosomes[1,2]. CIN can drive tumour heterogeneity and clonal evolution, and is thought to contribute to chemotherapy resistance in many cancer types including ovarian cancer[3,4]. Knowledge of the defective cellular pathways that underlie CIN would enable strategies to target cancer cells using synthetic lethal or CIN-limiting approaches[5], in addition to providing new diagnostic or prognostic tools. However, to date the causes of CIN in cancer remain ill-defined. Defective chromosome attachment to the mitotic spindle due to aberrant mitotic microtubule dynamics can contribute to CIN in cancer cell lines[6-9], potentially driven by alterations in spindle protein abundances[6] or genetic alterations in Aurora A, BRCA1 or Chk2[9]. Loss of retinoblastoma protein (pRB) leading to cohesion defects and CIN has been demonstrated in a sarcoma cell line[10]. Studies classifying CIN mechanisms in representative, cancer specific cell line panels are currently limited to colorectal cancer[8,11]where both DNA replication stress (the slowing or stalling of DNA replication) and elevated microtubule assembly rates were shown to contribute to CIN[8,11].

High-grade serous ovarian carcinoma (HGSC) represents an important clinical challenge; despite initial positive responses to first-line platinum therapy, most patients relapse, leading to a poor overall survival for this disease[12]. The genomes from both HGSC patient tumours[3,13,14] and ascites-derived HGSC cells[15] bear the scars of chromosomal instability as evidenced by highly aberrant genomic landscapes[3,13,14] (**Figure S1a**). There has been extensive interest in inferring potential cancer mutational mechanisms tumour and cancer cell line genomes, at both single nucleotide variant[16] and chromosome-scale aberrations, particularly in ovarian cancer[17,18]. However, apart from a high prevalence of mutations in homologous recombination (HR) genes,

and near ubiquitous *TP53* mutations[13], genetic drivers of CIN remain to be elucidated in HGSC. Moreover, it has been shown that BRCA-mutated tumours can acquire HR reactivating mutations[19], highlighting the need for functional analysis in defining ongoing CIN mechanisms. Genetic aberrations that may contribute to CIN in HGSC are Aurora A amplification and Cyclin E (*CCNE1*) amplification[20]. Overexpression of Cyclin E is linked to worse patient outcome[21] with combined high *CCNE1* expression and genomic amplification exhibiting higher genomic instability[22]. *RB1* mutations are also present in 17.5% HGSC tumours[14].

To date, functional characterisation using appropriate cell line models for HGSC is lacking. Recent advances including genomic approaches have defined multiple distinct subtypes of ovarian cancer, and have allowed the classification of available tumour-derived cell lines into suitable models[23-25]. We therefore undertook the first comprehensive functional characterisation of a curated panel of HGSC cell lines to define mechanisms driving chromosomal instability. We demonstrate that all cell lines exhibit extensive, ongoing CIN in the form of high rates of numerical and structural chromosome defects, and chromosome segregation errors. We find gross defects in multiple pathways controlling chromosome stability, and that either suppressing microtubule dynamics using low doses of paclitaxel, or limiting replication stress using nucleoside supplementation, reduces chromosome segregation errors and CIN. Furthermore, we show that functional analysis of CIN rates and types can inform sensitivity to standard therapies relevant to HGSC. In-depth genomic and gene expression analyses revealed potential genome stability regulators correlated with specific CIN mechanisms, or responses to therapy, providing a platform to investigate these associations in patient datasets. These new insights provide a first step towards designing new approaches to treat high-grade serous ovarian carcinoma, including determining whether limiting CIN could prevent CIN-driven chemotherapy resistance in HGSC[5], and guiding development of biomarkers for appropriate therapy choices.

Materials and Methods

Cell Lines: HGSC and fallopian cell lines were sourced as detailed in **Table S1** and maintained at 37°C and 5% CO_2. Their identities were confirmed by STR profiling (ATCC) . HCT116, SW620 (kind gift from C. Swanton) and Cov318 were maintained in DMEM High Glucose (Sigma); Kuramochi, G33, Ovkate, Ovsaho and Snu119 were maintained in RPMI (Sigma); All medium was supplemented with 10% FBS and 100 U Penicillin/Streptomycin. G164 cells were grown in DMEM F12 (Sigma) supplemented with 5% human serum (H4522, Sigma) and 100 U Penicillin/Streptomycin. FNE1/FNE2 were maintained in FOMI media (University of Miami)

supplemented with cholera toxin (C8052, Sigma). H2B-RFP stable cell lines were generated after transfection with lentiviral construct H2B-RFP (Addgene 26001) and flow sorting RFP-positive cells. Cells were routinely tested for mycoplasma using MycoAlert PLUS Mycoplasma Detection Kit (LT07-710, Lonza) and visual inspection using DAPI staining at the microscope. Cells were passaged for a maximum of 8-12 weeks (approx. 10-14 passages).

Proliferation assays: Cells were seeded into 96-well dishes. The next day, additional media was added, supplemented with either Embryomax nucleosides (final concentration of 10x) or low-dose paclitaxel (final concentration of 1 nM) or chemotherapy agents (at indicated final concentrations). Plates were imaged over the course of one week using an IncuCyte® live cell analysis system to calculate the percentage of confluency over time. The fold-change in confluency as a growth ratio (final confluency / starting confluency for that cell line grown under that condition) was reported.

Metaphase spreads: Cells were arrested in colcemid for two hours, collected then re-suspended in hypotonic solution (0.2% KCl, 0.2% Sodium Citrate) for 7 min at 37°C. Cells were pelleted and re-suspended in freshly-prepared 3:1 methanol-glacial acetic acid, then dropped onto slides.

Clonal FISH: Cells were seeded onto slides at low density to ensure growth of colonies from single cells. Colonies were grown with/without nucleosides for four weeks then fixed for fluorescence *in-situ* hybridisation (FISH). Cells in each colony were imaged and scored for centromere number, and percentage cells deviating from modal value for centromere of that colony was calculated.

Small molecule inhibitors: 100x Embryomax nucleosides (ES-008-D, Merck Millipore) were diluted in medium to 10x final concentration. Taxol (Paclitaxel, P045, Cambridge Bioscience) was dissolved in DMSO and used at 1 nM final concentration for low-dose rescue of CIN, or at higher doses for chemotherapy response. Monastrol (Sigma) was dissolved in DMSO and used at 100 μM. Olaparib (AZD2281, Gmbh) was dissolved in DMSO.

Immunofluorescence: Cells grown on coverslips were fixed with PTEMF (0.2% Triton X-100, 0.02 M PIPES (pH 6.8), 0.01 M EGTA, 1 mM $MgCl_2$, 4% formaldehyde). After blocking with 3% BSA, cells were incubated with primary antibodies according to suppliers' instructions. Antibodies were obtained from Abcam (Beta-tubulin (ab6046), CenpA (ab13939), Centrin 3

(ab54531), Cyclin A2 (ab16726), Hec1 (ab3613), RPA (ab79398)), Antibodies Incorporated (CREST (15-234-0001)), Bethyl Lab (Mad2 (A300 -300A)), Millipore (H2AX (05-636)), Santa Cruz (53BP1 (sc-22760) and Rad51 (sc-398587). Secondary antibodies used were goat anti-mouse AlexaFluor 488 (A11017, Invitrogen), goat anti-rabbit AF594, AF488 (A11012, A11008, Invitrogen), and goat anti-human AF647 (109-606-088-JIR, Stratech or A21445, Invitrogen). DNA was stained with DAPI (Roche) and coverslips mounted in Vectashield (Vector H-1000, Vector Laboratories).

FISH: Fluorescent *In Situ* Hybridisation was carried out according to manufacturer's instructions. In brief, cells on slides were fixed in 3:1 methanol:acetic acid, then put through an ethanol dehydration series (2 minutes in 70, 90, 100% ethanol) then air dried. Probe was added to slides which were heated to 72°C for 2 minutes, then left at 37°C overnight in a humid chamber. The next day, slides were washed in 0.25x SSC at 72°C for 2 minutes, then 2xSSC, 0.01% Tween at RT for 30 s. Slides were stained with DAPI then coverslips were mounted with Vectashield. Pan-centromere probe was purchased from Cambio (1695-F-02) and Centromere Enumeration Probes from Cytocell.

M-FISH: Metaphase spreads from each cell line were hybridised with the M-FISH probe kit 24XCyte (Zeiss MetaSystems) following the manufacturer's instructions. Briefly, the slides were incubated 30 minutes in 2xSSC buffer at 70°C, then allowed to cool at room temperature for 20 minutes. Following a 1 minute wash in 0.1XSSC, the cells were denatured in NaOH 0.07 M for 1 minute, then washed in 0.1xSSC, and 2xSSC. The cells were dehydrated in an ethanol series, and air dried. The probe mix was denatured at 75 °C for 5 min, and pre-annealed at 37°C for 30 min. 6 µl of probe mix were applied to each slide, under a 18x18mm coverslip. The slides were incubated for 3 days at 37°C, then washed for 2 minutes in 0.4xSSC, at 72°C, and 30 s in 2xSSC, 0.05% Tween20, at room temperature, and finally mounted in DAPI/Vectashield (VectorLabs). Images were acquired on an Olympus BX-51 microscope for epifluorescence equipped with a JAI CVM4+ progressive-scan CCD camera, and analysed using the Leica Cytovision Genus v7.1 software (Leica). A minimum of 25 metaphases were karyotyped for each cell line.

Fibre Assay: Fibres were prepared as described[26]. In brief, cells were pulse labelled with 25µM CldU and 250µM IdU (Sigma) for 20 min. Cells were harvested and then lysed using 0.5% SDS,

20mM Tris-HCl pH 7.4, 50mM EDTA. Fibres were spread on slides and DNA detected using rat anti-BrdU and CldU, with secondary antibodies as above.

Microscopy: Images were acquired using an Olympus DeltaVision RT microscope (Applied Precision, LLC) equipped with a Coolsnap HQ camera. Three-dimensional image stacks were acquired in 0.2 μm steps, using Olympus 100× (1.4 numerical aperture), 60× or 40× UPlanSApo oil immersion objectives. Deconvolution of image stacks and quantitative measurements was performed with SoftWorx Explorer (Applied Precision, LLC). H2B-RFP-labelled cells were live imaged in 4 well imaging dish (Greiner Bio-one). 20 μm *z*-stacks (10 images) were acquired using an Olympus 40× 1.3 numerical aperture UPlanSApo oil immersion objective every 3 min for 8 h using a DeltaVision microscope in a temperature and CO_2-controlled chamber. Analysis was performed using Softworx Explorer. Microtubule assembly assays (see below) were performed in part using an Eclipse Ti-E inverted microscope (Nikon) equipped with a CSU-X1 Zyla 4.2 camera (Ti-E, Zyla; Andor), including a Yokogawa Spinning Disk, a precision motorized stage, and Nikon Perfect Focus, all controlled by NIS-Elements Software (Nikon)).

Microtubule dynamics assay: Microtubule dynamics were analysed as described previously[8]. Briefly, assembly rates were calculated by tracking EB3-GFP protein foci in living cells. Cells were seeded onto glass-bottom dishes and transduced with virus containing pEGFP_EB3 (gift from S. Godinho) Cells were treated with Eg5 (Kif11) inhibitor monastrol (67 μM, Sigma) for 2 hr. Cells were then imaged on the DeltaVision microscope or using an Eclipse Ti-E inverted microscope (Nikon). Cells were imaged every 2 s using four sections with a Z-optical spacing of 0.4 μm. Average assembly rates (micrometres per minute) were calculated using data for 20 individual microtubules per cell for 10-20 cells.

Western blotting: Cell lysates were prepared using lysis buffer (20 mM Tris-HCl (pH 7.4), 135 mM NaCl, 1.5 mM $MgCl_2$, Triton 1%, Glycerol 10%, 1x Protease inhibitor (Roche)). Immunoblots were probed with antibodies against p53 (Santa Cruz sc126), Aurora A (Cell Signaling 12100), Vinculin (Cambridge Bioscience 66305) and cyclin E (Abcam ab3927) and developed using goat anti-mouse (Cell Signalling 7076S) or goat anti-rabbit (Santa Cruz sc-2004) IgG HRP conjugated antibodies, using a Chemidoc (GE Healthcare).

Rad51 response to IR: Cells were treated using an industrial cabinet X-ray device (RS-2000, Rad Source Technologies) for specific times calibrated to deliver 2Gy ionizing radiation and

then fixed after 2 or 24 h recovery before immunofluorescence with antibodies against Cyclin A and Rad51.

Flow cytometry: Cells were fixed in 4% formaldehyde for 7 min, permeabilised with 0.2% Triton X-100 for 2 min, stained with DAPI, and analysed using BD FACS Diva 8.2. RPE1 cells were used to calibrate FACS analysis to generate a profile for DNA signal peaks, corresponding to a diploid cell line. RPE1-H2B-RFP and parental RPE1 cells were then mixed and analysed together, for a direct comparison, to verify that H2B tagging did not alter the expected peaks. RPE1-H2B-RFP cells were then mixed with known near-diploid or aneuploid cell lines (HCT116 and SW1116) to verify that the FACS analysis could distinguish that RFP positive cells gave the expected profile compared to the RFP-negative cells when analysed together. RPE1-H2B-RFP cells were then mixed with individual HGSC cell lines, to determine whether each HGSC cell line overlapped the diploid DNA signature or differed, indicating aneuploidy.

Whole Genome Sequencing: Sample processing and whole genome sequencing were carried out by Edinburgh Genomics. Samples were processed using Illumina TruSeq Nano libraries. and sequenced with Illumina HiSeq X instruments to an average depth coverage of 30X. Due to the nature of our cell line samples, matched normal tissue/blood samples were unavailable for analysis. For further details including downsampling and absolute copy number estimation, somatic mutation and copy number variation, and cancer genome breakpoint analysis methods see **Supplementary Methods**.

RNAseq Analysis: RNA was extracted from cell lines using RNEasy kits (Qiagen) for three biological repeats. RNA-seq was performed by Bart's and the London Genome Centre on the Illumina NextSeq 500 platform, generating on average ~1.5 million single-end reads of 75 bp in length per sample. For analysis methods see **Supplementary Methods**.

Statistical Analysis: Statistical tests were carried out where indicated in figure legends, as either an unpaired t-test with Welch's correction, or a one-way ANOVA with Dunnett's multiple comparison (every cell line compared to FNE1). Asterisks denote the significance value between experimental conditions adhering to the following nomenclature: $p<0.05$ (*); $p<0.01$ (**); $p<0.001$ (***); $p<0.0001$ (****). For values close to $p=0.05$, actual p-values are given. All calculations were carried out using software (Graphpad Prism 8.0).

Results

Numerical and structural chromosome defects, and persistent chromosome segregation errors in HGSC cell lines.

Cancer-derived cell lines have proven a useful resource to investigate ongoing mechanisms driving chromosomal instability[6,8,11,27]. We assembled a panel of seven HGSC lines, five from the top ten suitable cell line models for HGSC (Cov318, Kuramochi, Ovkate, Ovsaho, Snu119)[23] and two obtained from recent confirmed HGSC patients (G33[28] and G164) (**Table S1**). As tissue-type specific controls, we obtained two, h-TERT-immortalised fallopian tube serous epithelial cell lines (FNE1 and FNE2[29]), representing the likely tissue of origin of HGSC[30]. We performed whole genome sequencing (Methods) to characterize the extent of genomic alteration in the HGSC lines. First, to visualise genomic gains and losses, we performed copy number segmentation and computed the DNA copy number profiles (**Figure 1a**; see Methods for details). Similar to HGSC genomes available in the TGCA dataset[13,23], the HGSC lines displayed complex copy number profiles (**Figure 1a**). Our analysis also computed the most likely models of ploidy (**Figure S1b**), and we further confirmed these using chromosome counting from metaphase chromosome spreads (**Figure 1b,c, Figure S1c**) and FACS ploidy analyses (**Figure S1d**). There was a notable range in ploidy between cell lines, varying between near-diploid (2n) to near-tetraploid (4n) (**Figure 1c**). To examine chromosome alterations at a single-cell level, we performed multiplex-FISH (M-FISH) on metaphase chromosome spreads for FNE1 and Kuramochi cell lines. As expected, FNE1 were near diploid (**Figure 1d; Table S1**). By contrast, Kuramochi cells displayed a high prevalence of numerical and structural alterations that were highly heterogeneous between individual cells (**Figure 1d** and **Figure S1e**). Metaphase chromosome spreads analysed with centromeric fluorescence *in-situ* hybridisation (FISH) probes also demonstrated the presence of structural chromosome aberrations (dicentric and acentric chromosomes) in all HGSC cell lines (**Figure S1f**).

We next analysed genetic mutations relevant to HGSC. We verified the known *BRCA2* non-sense mutation in Kuramochi[23], but did not identify any *BRCA1/2* mutations of known pathogenicity in other cell lines (**Table S2; Figure S5a**). Some lines exhibited *BRCA1* or *BRCA2* copy number alteration (**Figure S1j**) although gene expression was not significantly altered compared to the FNE controls except for *BRCA2* in Ovsaho (**Figure S1g, S5c**). *TP53* mutations occur in 96% of HGSC tumours[13]. Accordingly, all seven HGSC cell lines exhibited *TP53* mutations and aberrant p53 protein expression (including premature stop codons in G33 and Ovsaho) compared to FNE1 cells (**Figure S1h,j, Table S2**). Five cell lines demonstrated *CCNE1* copy number gain and corresponding changes in RNA expression, and all seven lines showed

overexpression at protein level compared to FNE1 (**Figure S1i,j**). Our HGSC cell line panel thus recapitulates key genomic features of HGSC tumours, and encompasses a range of ploidy and genomic alterations.

The diversity of chromosome alterations between individual Kuramochi cells, and the prevalence of structural and numerical chromosome alterations in all HGSC lines, suggested that chromosomal instability was ongoing. Indeed, live cell imaging of cell lines stably expressing mRFP-tagged Histone H2B revealed the frequent occurrence of chromosome mis-segregation events in all HGSC cell lines (**Figure 1e,f**). Chromosome segregation errors were further examined using high-resolution imaging of fixed cells to gain insights about the nature of mis-segregating chromatin (**Figure g-i**). Anaphase lagging chromatin was sometimes negative for CREST-reactive serum (marks centromeric proteins) and Hec1 kinetochore proteins, suggesting that some mis-segregation events were precipitated by structural chromosome alterations (**Figure 1g,i,j**). To verify the acentric nature of lagging chromatin, we performed FISH using all-centromere-targeted probes in the G33 cell line. This confirmed the presence of mis-segregating chromatin devoid of centromeric DNA sequence (**Figure 1k,l)**. We were struck by the high frequency of chromosome mis-segregation in some lines, for example Cov318 exhibited errors in 50% of cells, with each cell typically displaying multiple errors, often of different types (**Figure 1j**). HGSC cell lines thus exhibit continual mis-segregation of both intact and structurally abnormal chromosomes, contributing to their high rates of numerical and structural CIN.

HGSC cell lines exhibit pronounced chromosome congression delays, a functional mitotic checkpoint and normal sister chromatid cohesion.

We next tested whether control of mitosis was perturbed in HGSC, by analysing mitotic progression kinetics using live cell imaging. Slight congression delays have been reported in colorectal cancer[8] but it was hitherto unknown whether this occurs in other cancer types. Four HGSC cell lines exhibited significant delays in mitosis, as measured by both the time from nuclear envelope breakdown to anaphase onset (**Figure 2a,b**) and the time from chromosomal congression to the metaphase plate (**Figure 2c**) There was no obvious correlation between higher cell line ploidy and slowed congression, suggesting this phenomenon is unconnected with the number of chromosomes present. The overall prolonged time in mitosis suggested that congression errors were capable of mounting a robust mitotic checkpoint response. Accordingly, live cell imaging revealed that all of the four HGSC cell lines tested were able to efficiently arrest mitosis following treatment with nocodazole to depolymerise all microtubules **(Figure**

2d). Moreover, immunofluorescence revealed the expected presence of two key mitotic checkpoint proteins, Mad2 and BubR1, on uncongressed chromosomes in all cell lines tested (**Figure S2a,b**). Prolonged delays in mitosis have been linked to defective sister chromatid cohesion and chromosome mis-segregation[32]. To evaluate this, we measured inter-centromere distance, which provides a measure of sister chromatid cohesion defects[33]. This suggested chromosome cohesion was normal in all HGSC lines with the possible exception of Cov318 (**Figure S2c,d**). We note that it was not possible to directly assess cohesion fatigue in these cell lines as their slow chromosome congression rates confound these analyses.

Aberrant microtubule assembly rates contribute to chromosome segregation errors in HGSC.

The significant delays in chromosome congression, and the presence of some apparently whole (centric), lagging chromosomes in anaphase (**Figure 1i, 2c**) suggested that the mitotic machinery was disrupted in HGSC. Centrosome abnormalities have been detected in ovarian cancer[27], and can promote the formation of multipolar spindles[34]. Although multipolar spindles can resolve to a pseudo-bipolar spindle in a process known as centrosome clustering[35], this can elevate the frequency of incorrect chromosome attachments to the spindle and increase chromosome segregation errors[34,36]. We therefore quantified centrosome and spindle defects from mitotic cells using antibodies against centrioles (centrosome cores; two per centrosome). Most cell lines exhibited a significant percentage of cells with supernumerary (>4) centrioles (**Figure S3a,b**). Cell lines with extra centrosomes also displayed multipolar spindles in prometaphase cells (**Figure S3c,d)**. Multipolar spindles usually resolved to pseudo-bipolar spindles by anaphase, since most cells underwent bipolar cell division (**Figure S3e).** To investigate whether centrosome amplification was associated with elevated chromosome segregation errors in HGSC, we compared error rates between anaphase cells with 4, or more than 4 centrioles. In the two lines tested, (G33 and G164), the presence of extra centrosomes tended to correlate with a higher rate of chromosome segregation errors, although this was only statistically significant for G164 (**Figure S3f,g**), suggesting a potential small contribution of extra centrosomes to CIN in HGSC.

Elevated microtubule (MT) dynamics leading to delayed chromosome congression, chromosome segregation errors and CIN were recently described in colorectal cancer as a result of either Aurora A overexpression[8] or the deregulation of the Chk2-BRCA1 axis[9,37]. Our panel of HGSC cell lines carries potential Aurora A defects due to a common amplification of the chromosomal region carrying the Aurora A gene (*AURKA*, 20q[23]; **Figure 1a**; **Figure S3h)**, that

is also common in HGSC tumours[23]. Indeed, Aurora A levels were upregulated at both transcriptional and protein level in all our cell lines (**Figure S3i**). We therefore tested whether MT dynamics were altered in HGSC cell lines, by transiently expressing the MT tip-tracking protein EB3 tagged with GFP and filming MT growth. To allow accurate quantification of mitotic spindle MT dynamics, this assay was carried out in cells treated with the Eg5 inhibitor Monastrol to generate monopolar spindles, as previously described[8] (**Figure 2e** and **Movie S1**). We included the colorectal cancer cell lines HCT116 (CIN-negative) and SW620 (CIN-positive) as controls for normal, and elevated MT assembly rates respectively[8]. MT assembly rates were significantly elevated compared to FNE1 cells in all HGSC cell lines except Kuramochi (**Figure 2f**) with most lines notably displaying mean MT assembly rates well above CIN-positive SW620 colorectal cancer cells. We sought to determine whether this phenomenon was causative for CIN in HGSC. We treated cells with a low dose of the MT stabilising agent, paclitaxel (Taxol), previously demonstrated to suppress MT assembly rates in colorectal cancer cell lines[8]. It has been previously established that monopolar mitotic spindles frequently orient asymmetrically when MT assembly is elevated[38], thus providing a proxy read out for elevated MT assembly rates. All seven HGSC lines demonstrated asymmetric monopolar spindles at a higher incidence than the FNE2 control, which was reduced when cells were treated with low dose paclitaxel (**Figure 2g, h**), and rescue of abnormal MT dynamics was directly confirmed for two cell lines using the EB3-GFP tip tracking assay (**Figure 2i**). Reducing abnormal MT dynamics also reduced chromosome segregation errors in all five HGSC cell lines tested (**Figure 2j,k**) independent of any effect on proliferation (**Figure S3j**), similar to the effect in colorectal cancer cell lines[8]. This demonstrates that, for this HGSC cell line panel, aberrant MT dynamics contribute to chromosome mis-segregation and that low dose paclitaxel represents a viable strategy for experimentally reducing CIN in HGSC.

Replication stress contributes to chromosome mis-segregation and CIN in HGSC

Replication stress, the slowing or stalling of DNA replication, is known to occur in multiple cancer types[39,40] and was previously shown to contribute to CIN in colorectal cancer by generating acentric fragments and chromatin bridges[11]. The presence of acentric lagging chromatin, structural chromosome defects, and the known roles of homologous recombination proteins frequently mutated in HGSC (such as BRCA1 and BRCA2) in protecting the DNA replication fork[41-43], suggested that HGSC cell lines may experience replication stress. To test this, we directly examined replication fork speed using single DNA fibre pulse-labelling. All HGSC cell lines exhibited reduced replication fork rates compared to control FNE1 cells (**Figure**

3a). We next examined whether this reduced fork speed would correlate with known hallmarks of replication stress, namely; elevated prometaphase DNA damage as indicated by γH2AX foci, 53BP1 bodies in G1 cells and ultrafine anaphase bridges[11,44]. Most cell lines exhibited elevated levels of γH2AX, but increased levels of ultrafine bridges or formation of 53BP1 bodies were seen in only a few cell lines (**Figures 3b-d**).

We next examined whether elevated replication stress contributes to chromosome mis-segregation and CIN in HGSC, by reducing replication stress using nucleoside supplementation as previously described[11,45]. This reproducibly reduced segregation errors compared to untreated cells in three cell lines (Ovsaho, Cov318 and G164). By contrast, Snu119, Kuramochi and G33 were overall non-responsive (**Figure 3e,f, S4**). To test whether suppression of replication stress could translate into a reduction in karyotypic heterogeneity, we grew colonies from single cells and performed centromeric FISH to measure within-clone deviation in centromere number. Replication stress does not generally induce whole chromosome mis-segregation, and can cause preferential mis-segregation of specific chromosomes[46]. Moreover, HGSC cell lines frequently demonstrated multiple error types per cell (**Figure 1j**) and we therefore expected a weak, if any, reduction in centromere number deviation. Nonetheless, Ovsaho and Kuramochi displayed reduced karyotypic heterogeneity for one or both chromosomes scored following single cell colony derivation in the presence of nucleosides (**Figure 3g,h**). Cov318 did not show a reduction in colony mode deviation despite reduced chromosome segregation errors. Effects of nucleoside supplementation on chromosome segregation and karyotypic heterogeneity were independent of any effects on proliferation (**Figure S3j**). Taken together, these data demonstrate the presence of replication stress that contributes, in at least a subset of lines, to chromosome segregation errors and CIN in HGSC. However, the manifestation of the canonical hallmarks of replication stress, and the response to nucleoside supplementation, varied between cell lines.

We wondered if this variation could be explained by differences in responses to replication stress. We tested this by treating cells with low doses of the DNA polymerase poison aphidicolin to provide exogenous replication stress[44]. Cov318 cells had high basal levels of 53BP1 bodies that were further elevated in response to aphidicolin, whereas Kuramochi, Ovkate and G33 cells failed to recruit 53BP1 in response to both their endogenous and exogenous replication stress (**Figure 3c,i,j**). This suggests that some HGSC cell lines may either have an increased capacity to repair stalled forks before they result in damage, or a failure in labelling replication stress-induced DNA damage via the canonical pathway observed in model cellular systems[44] and other cancers[11].

Differences in CIN mechanisms can indicate responses to HGSC therapeutics.

PARP inhibitors recently emerged as a new therapy to treat cancers with homologous recombination repair deficiencies (HRD) caused by mutations in HR genes such as BRCA1/2[47]. Given that many of the HGSC cell lines demonstrated replication stress that might result in increased stalled forks, we wondered if this might result in sensitivity to PARP inhibitors. We therefore treated all cell lines with a range of olaparib doses and monitored cell growth using IncuCyte® cellular imaging **(Figure 4a).** Most HGSC cell lines demonstrated similar sensitivity to FNE1 cells (proliferation reduced by 50% at 1-10μM olaparib). However, G33 and Ovkate were more resistant suggesting a differential HR capability between these and the other HGSC cell lines. We therefore directly tested cellular responses to ionising radiation using a Rad51 focus formation time-course assay, a common measure of HR efficiency[48,49] (**Figure 4b**). FNE1 cells showed an increase in Rad51 foci within two hours, and by 24 hours, foci began to decrease in number (**Figure 4c**). This pattern was recapitulated in all HGSC cell lines, with the notable exception of G33, that showed a marked delay in formation of Rad51 foci (**Figure 4c**). Collectively these data suggest that the relative resistance of G33 and Ovkate to olaparib was not due to HRD-induced sensitivity in the other cell lines. A delayed Rad51 response in G33 cells may therefore reflect a general failure of replication stress and/or DNA damage response rather than HR capability directly. We observed reduced replication stress responses (such as low γH2AX and 53BP1 foci despite reduced replication fork speeds, and failure to induce 53BP1 foci upon aphidicolin treatment) in G33 and Ovkate (see **Figure 3b,c,j**). We suggest that an attenuated replication stress response might therefore serve as a novel indicator of resistance to PARP inhibitor therapy.

Paclitaxel is a mainstay chemotherapy agent used to treat HGSC patients, but can be very neurotoxic[50]. There are currently no biomarkers for which patients would benefit most from paclitaxel as a chemotherapy. Since paclitaxel stabilises MTs, we reasoned that cell lines with elevated MT assembly rates might be inherently resistant to paclitaxel. Indeed, Kuramochi, the cell line that exhibits near-normal MT assembly rates (see **Figure 2f**) was the most sensitive to paclitaxel, with a proliferation response similar to FNE1 and FNE2 (**Figure 4d**). Other cell lines showed increasing resistance to paclitaxel that positively correlated with their MT assembly rates although this did not reach significance (**Figure 4e**). This suggests that methods to assess elevated MT assembly rates in cancer patient samples could be further explored as an indicator for paclitaxel effectiveness.

Genetic and transcriptomic analyses reveal potential causative CIN genes.

Given the links between functional CIN readouts and chemotherapy sensitivities we were motivated to thoroughly assess whether genomic, genetic or transcriptomic analyses (more readily available from patient samples) might indicate these key CIN features, and also shed light on the precise deregulated pathways culminating in the observed functional phenotypes. For this purpose, we performed single nucleotide variant (SNV) calling using the Genome Analysis Toolkit (GATK) workflow, utilizing a Panel of Normals (PoN) to stringently remove common single nucleotide polymorphisms (SNPs), as matched normal samples were not available. We thus identified a list of likely somatic mutations (**Table S2**;**Figure S5a**). Most cell lines carried two to seven potentially CIN-related mutations, however none of these obviously co-segregated with specific phenotypes (**Figure S5a**). G33 bore thirteen mutations in potential CIN-genes, although the overall genome mutation rate was similar to the other HGSC cell lines (**Figure S5b**). Next, we analysed the transcriptome of each cell line using RNA sequencing. We collated all significantly altered CIN-related genes (**Table S3**;**Figure S5c**). Of these, *RB1, TopBP1*, *CCNE1* (Cyclin E), and genes from MCM and GINS DNA replication complexes were frequently deregulated (**Figure S5c**). We noted that G33 was the only cell line to show significant elevated expression of 53BP1. We also looked for gene expression changes that were linked to particular phenotypes. For PARP inhibitor resistance (**Figure 4a**), we examined genes whose expression was altered (relative to both FNE1 and 2) in both Ovkate and G33, but not altered in the five HGSC cell lines that showed olaparib sensitivity (**Figure S5d**). We found no statistically significant gene ontology pathway enrichment, however we did note that there were five significantly altered genes with DNA replication and repair functions (**Figure S5d**). One of these was TLK1, a kinase responsible for assembly of nucleosomes on replication forks with a potential role in PARP inhibitor response[51]. Similarly, an analysis of the cell lines with strongest paclitaxel resistance (**Figure 4d**) revealed a cluster of eight genes involved in microtubule regulation, and five DNA replication-related genes were commonly altered in cell lines with an attenuated response to replication stress (**Figure S5d**). When comparing between cell lines with differential responses to nucleoside-mediated segregation error rescue (**Figure 3f**), we found an enrichment in genes regulating nucleotide metabolism, which might explain why some cell lines had better CIN reduction than others. For the congression defects observed in four cell lines (**Figure 2c**), the most relevant significantly enriched pathway was actin cytoskeleton reorganisation (**Figure S5d**). As well as concentrating on known CIN-related pathways, we also identified the significantly altered genes and pathways in those HGSC cell lines sharing specific

CIN phenotypes, analysed independently from the FNE controls (**Figure S6a,b**, **Table S4**). Overall genetic and transcriptomic analysis did not reveal any clear causative pathways to CIN, but these data provide a resource for future identification of genes related to those phenotypes, and to potentially identify novel roles in CIN for other genes.

Discussion

Here we have performed the first systematic and comprehensive functional analysis of mechanisms driving chromosomal instability in a panel of representative HGSC cell lines. All seven lines demonstrate extensive ongoing CIN in the form of chromosome mis-segregation that is associated with multiple mechanisms, including elevated microtubule assembly rates, centrosome amplification, and replication stress (see **Figure 5** for a summary and correlations between phenotypes across all cell lines). A striking finding of our study is that compared to colorectal cancer cell lines, HGSC cell lines exhibit a greater number of co-operating CIN mechanisms, and each CIN mechanism often operates at more extreme levels (for example slower replication fork rates and higher MT assembly rates than colorectal cancer cell lines). Moreover, multiple CIN mechanisms likely exist within single HGSC cells as evidenced by the presence of chromosome segregation errors of multiple types per cell (**Figure 1g-j**). This complexity explains the partial reductions in CIN obtained using CIN limiting experiments (low dose paclitaxel and nucleoside supplementation), and will be important to consider when designing approaches to target CIN therapeutically in this disease. We also noted that HGSC lines were not entirely uniform in the extent to which each CIN mechanism was manifested. Interestingly we discovered that these differences in characteristics or severity of specific CIN mechanisms were related to sensitivity to paclitaxel and PARP inhibition, mainstays of HGSC treatment. Whole genome sequencing and transcriptomic analysis revealed potential genetic drivers of CIN in HGSC that can be harnessed in future mechanistic studies. Given these findings we suggest that assessing CIN mechanisms in HGSC patients either functionally or by association with specific mutational or transcriptomic signatures may provide new biomarkers to predict sensitivity to paclitaxel and PARP inhibitors.

Centrosome amplification has been observed in many cancer types, although its origin is still unclear. Whole genome doubling (WGD) events caused by cytokinesis failure could generate both centrosome amplification and increases in chromosome ploidy. Indeed, WGD is estimated to occur particularly frequently in HGSC[52]. However, many cells exhibited centriole numbers exceeding eight (the expected consequence of cytokinesis failure) (**Figure S3g**) and some centrosome amplified lines were close to diploid (e.g. Kuramochi), suggesting potential

alternative routes to centrosome amplification. One such cause could be replication stress itself, since slow replication can cause extra centrosomes[53]. Centrosome amplification correlated with increased segregation errors in the cell lines tested, but cells with normal centriole numbers also exhibited high error rates, suggesting this is not the main driver of CIN in HGSC (**Figure S3f**).

Most HGSC lines displayed defects in chromosome congression, and all cell lines except Kuramochi exhibited markedly elevated microtubule assembly rates. Notably, all of the cell lines we tested demonstrated significantly reduced segregation errors after treatment with low doses of paclitaxel to restore aberrant MT assembly (**Figure 2k**) suggesting this is a major contributor to HGSC CIN. In colorectal cancer, elevated MT assembly rates are proposed to occur as a result of overactive Aurora kinase A[9,37] or a deregulated BRCA1-Chk2 axis[8,9]. None of our eight cell lines exhibited *BRCA1* point mutations. Some lines displayed evidence of partial *BRCA1/2* copy number loss but we saw no significant reduction in BRCA1/2 expression at the RNA level except in Ovsaho (**Figure S1g,j, S5c**). All lines except Snu119 however, displayed copy number gain of the *AURKA* locus (**Figure S3h,i**), and all cell lines showed Aurora Kinase A overexpression at mRNA and protein level, suggesting that in this panel at least, *AURKA* gene amplification may be a key driver of MT over-assembly, mitotic abnormalities and CIN in HGSC. However, despite displaying Aurora Kinase A upregulation, Kuramochi did not exhibit significantly elevated MT assembly rates. Kuramochi was also notably the most sensitive to higher, clinically-relevant doses of paclitaxel. Discovering the cause of these differential phenotypes and whether functional biomarkers could be derived (such as a clinical measure of MT assembly rates) may lead to the first clinical biomarker for paclitaxel sensitivity.

It is also possible that other genetic lesions could generate elevated MT assembly rates, for example DNA-PKcs has recently been identified as upstream of the BRCA1-Chk2 axis[54]. Cep72 has been implicated in MT assembly defects[41] and is significantly overexpressed in Ovkate. Moreover, comparison of transcriptomic features of cell lines that were most affected by congression delays identified an enrichment of eleven genes in actin reorganisation, that might indicate a systemic cytoskeletal defect. Supernumerary centrosomes could also contribute to elevated MT assembly rates as a result of increased MT nucleation[55], suggesting the intriguing possibility that extra centrosomes might mediate chromosome mis-segregation via mechanisms over and above their canonical role in promoting abnormal geometry during spindle formation. Lastly, a connection between replication stress and elevated MT assembly rates has also been described in colorectal cancer [56] and it would be interesting to examine this further in HGSC.

Alongside mitotic defects, all seven HGSC cell lines also exhibited some degree of replication stress, as evidenced from single molecule DNA fibre analysis and other hallmarks of

replication stress. Oncogene-induced replicative and mitotic stress can result from a myriad of known oncogenes and tumour suppressor genes[57,58] however HGSC harbours relatively few recurrent mutations. Similarly, our panel of cell lines shared few mutations in common (**Figure S5a**), with the exception of *TP53*. Cyclin E has been noted as a common defect in HGSC[20]. Five cell lines showed *CCNE1* amplification at gene level, six had significantly increased RNA expression and all showed increased protein expression (**Figure S1i**); however this did not seem to correlate with any of the specific replication stress phenotypes we investigated herein and may simply play a role in promoting replication stress and CIN in general in HGSC[59] (**Figure 5**). Replication stress has been successfully treated with exogenous nucleoside supplementation in a variety of models[11,45,60,61]. We found that nucleosides had a positive, or at worst only neutral, effect on segregation errors in HGSC cell lines. Crucially we saw no negative effect in the FNE1 control. This suggests that nucleoside supplementation could be investigated further, perhaps as a prophylactic treatment for women with familial risk of developing HGSC, or given alongside therapy in order to reduce the likelihood of developing treatment-resistant disease.

Unexpectedly, many of the cell lines did not entirely follow the canonical response[11,44] to replication stress. G33 and Ovkate were among those cell lines particularly unusual in lacking multiple replication stress markers including γH2AX and 53BP1 bodies and when further challenged with aphidicolin, both remained incapable of mounting a DNA damage response (**Figure 3b,c,j**). Strikingly, these two cell lines were resistant to PARP inhibition compared to other cell lines and the FNE controls. Moreover, this was connected, in the case of G33, to a defective Rad51 recruitment to IR-induced DNA damage which would normally be taken to indicate HR deficiency. All other cell lines recruited Rad51 with normal kinetics. In line with this there was no significant loss of expression at RNA level of known HR genes (except for *RAD51D* in Kuramochi and *BRCA2* in Ovsaho; **Figure S5c**) despite the reduced copy number of BRCA1 and 2 in multiple cell lines and the known mis-sense mutation detected in Kuramochi[23] (**Figure S1g,j, S5a,c)**. Originally the success of PARP inhibitors was attributed to the synthetic lethality involved in disabling the break excision repair function of the PARP pathway, leaving HRD tumours unable to repair single stranded DNA breaks. More recent work has pointed to an increased complexity of possible mechanisms, with PARP inhibition resulting in stalled replication forks that cannot be restarted in a BRCA-minus background, and thus become vulnerable to degradation due to excessive MRE11 nuclease activity[62]. New 'backup' pathways have also been described in cancer cells, such as reliance on Rad52 to promote Rad51 loading in BRCA-deficient cells[63], or the downregulation of PTIP to reduce MRE11

recruitment[62]. Since replication stress is also likely to result in stalled forks that need repair or restart, these different pathways to stalled fork resolution may also underpin the variation in replication stress response observed within our HGSC cell line panel. It will be interesting to test whether inhibition of Rad52 would re-sensitise G33 and Ovkate to PARP inhibition. These studies, alongside our findings that G33's delayed Rad51 focus formation correlated with PARP inhibition resistance rather than sensitivity, suggest that consideration of replication stress levels and responses may also need to be taken into consideration when predicting clinical PARP inhibitor sensitivity, and when interpreting functional assessments of HR competency.

G33 carried the highest number of mutations in known CIN-related genes (**Figure S5a**). We also noted that G33 was the only cell line to show elevated gene expression of 53BP1 despite an inability to form 53BP1 bodies (**Figure 3j, S5c**), which might lead to an imbalance in the non-homologous end joining/HR responses to DNA damage and contribute to PARPi resistance. Intriguingly, G33 is also the only cell line with significant loss of p53 expression at both RNA (**Figure S5c**) and protein (**Figure S1h**) levels, whereas the other cell lines expressed mutant alleles of full length or truncated (Ovsaho) protein. Loss of p53 expression has previously been linked with aberrant Rad51 recruitment[64] and G33's non-sense allele (W146*) has been observed in a subset of HGSC patients[65]. It would be worth investigating the extent to which this mutation plays a role in G33's unique phenotypes both experimentally and in clinical datasets.

The lack of matched normal patient DNA samples made some genetic analyses difficult. Herein we used various approaches to circumvent this issue. However, future studies will benefit from the acquisition of patient-specific matched normal DNA samples to permit more extensive analyses to link genotype to CIN phenotypes. Another potential caveat of this study is that there may be differences in the behaviour of cell line models compared to cells within tumours in patients. To mitigate against this, we selected a panel of HGSC cell lines whose genetic and genomic features recapitulated HGSC tumours[23-25]. We also enhanced the strength of our analysis by comparing our RNA expression profiles and CIN phenotypes not just between cancer cell lines but also against two appropriate, tissue-specific control cell lines. Moreover, the behaviour of this cell line panel was notably different to previously characterised colorectal cancer cell line panels that did not display overt chromosome congression delays or supernumerary centrosomes[8,11]. Therefore, tumour-derived cell lines still represent the best currently available model to functionally connect genetic lesions, genomic alterations and CIN mechanisms. Moreover, a landmark study has recently shown extensive cell division abnormalities from patient-derived HGSC cancer cells, at similar rates to what we have observed in our cell lines[15]. This provides an important complementary validation of our findings, and

suggests the CIN mechanisms identified herein are likely to be *bona fide* HGSC CIN mechanisms, that can be validated *in vivo* in future studies.

This study provides new understanding of the nature of CIN in HGSC, is directly comparable to existing knowledge of CIN mechanisms in other cancer types, and moreover lays the groundwork for future studies to validate mechanisms driving HGSC CIN *in vivo*. Our findings also have the potential to facilitate future research into synergising with patient-specific CIN mechanisms as a therapeutic strategy.

Author contributions

NT and NS performed most experiments and analysis. JM contributed to MT assembly rate experiments and centrosome quantification. TS performed western blots for AurKA and Cyclin E, and performed experiments in Figure 2d. DMu performed bioinformatic analysis supervised by KC. EM analysed transcriptional changes from RNAseq, supervised by JW. DMo and MD performed and analysed M-FISH experiments supervised by CG. FB provided cell lines and intellectual input and advice throughout the study. SM conceived the experimental design and supervised all experimental work and analysis. NT, NS and SM wrote and edited the manuscript.

Acknowledgements

We would like to thank Professor D. Bowtell for intellectual input and sharing of unpublished data, Professor C. Swanton for the kind gift of SW620 and HCT116 cell lines and S. Godinho for the kind gift of EB3-GFP constructs. We thank R. Basto and S. Taylor for sharing unpublished data and helpful discussions. We would also like to thank all members of the McClelland laboratory for useful discussions and reading of the manuscript. We thank the CRUK Flow Cytometry Core Service at Barts Cancer Institute (Core Award C16420/A18066). We acknowledge Dr Tan A. Ince, Live Tumor Core (LTCC) at University of Miami for FNE1 and FNE2 cell lines.

Grant support

NT was funded by Barts Charity (487/2133) and a Wellbeing of Women project grant (RG2040). DMu and TS were funded by a Wellbeing of Women project grant (RG2040). NS was funded by the Pancreatic Cancer Research Fund (PCRF) and a CRUK Pioneer Award (C35980/A27846). CMG, DMo and MAD were funded by Wellcome core award (090532/Z/09/Z). FB was funded by European Research Council (ERC322566) and Cancer Research UK (A16354, A25714). EM and JW acknowledge support from Cancer Research UK Centre of Excellence Award to Barts Cancer Centre (C16420/A18066). KC was funded by a UKRI Rutherford Research Fellowship.

Supplementary materials

(one supplemental movie, four supplemental tables, six supplemental figures)

References

1 Lengauer, C., Kinzler, K. W. & Vogelstein, B. Genetic instability in colorectal cancers. *Nature* **386**, 623-627, doi:10.1038/386623a0 (1997).

2 Lengauer, C., Kinzler, K. W. & Vogelstein, B. Genetic instabilities in human cancers. *Nature* **396**, 643-649, doi:10.1038/25292 (1998).

3 Bashashati, A. *et al.* Distinct evolutionary trajectories of primary high-grade serous ovarian cancers revealed through spatial mutational profiling. *The Journal of pathology*, doi:10.1002/path.4230 (2013).

4 Castellarin, M. *et al.* Clonal evolution of high-grade serous ovarian carcinoma from primary to recurrent disease. *The Journal of pathology* **229**, 515-524, doi:10.1002/path.4105 (2013).

5 McClelland, S. E. Role of chromosomal instability in cancer progression. *Endocrine-related cancer* **24**, T23-T31, doi:10.1530/ERC-17-0187 (2017).

6 Bakhoum, S. F., Genovese, G. & Compton, D. A. Deviant kinetochore microtubule dynamics underlie chromosomal instability. *Current biology : CB* **19**, 1937-1942, doi:10.1016/j.cub.2009.09.055 (2009).

7 Thompson, S. L. & Compton, D. A. Chromosome missegregation in human cells arises through specific types of kinetochore-microtubule attachment errors. *Proceedings of the National Academy of Sciences of the United States of America* **108**, 17974-17978, doi:10.1073/pnas.1109720108 (2011).

8 Ertych, N. *et al.* Increased microtubule assembly rates influence chromosomal instability in colorectal cancer cells. *Nature cell biology* **16**, 779-791, doi:10.1038/ncb2994 (2014).

9 Ertych, N., Stolz, A., Valerius, O., Braus, G. H. & Bastians, H. CHK2-BRCA1 tumor-suppressor axis restrains oncogenic Aurora-A kinase to ensure proper mitotic microtubule assembly. *Proceedings of the National Academy of Sciences of the United States of America* **113**, 1817-1822, doi:10.1073/pnas.1525129113 (2016).

10 Manning, A. L. *et al.* Suppression of genome instability in pRB-deficient cells by enhancement of chromosome cohesion. *Molecular cell* **53**, 993-1004, doi:10.1016/j.molcel.2014.01.032 (2014).

11 Burrell, R. A. *et al.* Replication stress links structural and numerical cancer chromosomal instability. *Nature* **494**, 492-496, doi:10.1038/nature11935 (2013).
12 Vaughan, S. *et al.* Rethinking ovarian cancer: recommendations for improving outcomes. *Nature reviews. Cancer* **11**, 719-725, doi:10.1038/nrc3144 (2011).
13 Bell, D. A. Integrated genomic analyses of ovarian carcinoma. *Nature* **474**, 609-615, doi:10.1038/nature10166 (2011).
14 Patch, A. M. *et al.* Whole-genome characterization of chemoresistant ovarian cancer. *Nature* **521**, 489-494, doi:10.1038/nature14410 (2015).
15 Nelson, L. *et al.* A living biobank of ovarian cancer ex vivo models reveals profound mitotic heterogeneity. *Nature communications* **11**, 822, doi:10.1038/s41467-020-14551-2 (2020).
16 Alexandrov, L. B. *et al.* Signatures of mutational processes in human cancer. *Nature* **500**, 415-421, doi:10.1038/nature12477 (2013).
17 Macintyre, G. *et al.* Copy number signatures and mutational processes in ovarian carcinoma. *Nature genetics* **50**, 1262-1270, doi:10.1038/s41588-018-0179-8 (2018).
18 Wang, Y. K. *et al.* Genomic consequences of aberrant DNA repair mechanisms stratify ovarian cancer histotypes. *Nature genetics* **49**, 856-865, doi:10.1038/ng.3849 (2017).
19 Sakai, W. *et al.* Functional restoration of BRCA2 protein by secondary BRCA2 mutations in BRCA2-mutated ovarian carcinoma. *Cancer research* **69**, 6381-6386, doi:10.1158/0008-5472.CAN-09-1178 (2009).
20 Etemadmoghadam, D. *et al.* Integrated genome-wide DNA copy number and expression analysis identifies distinct mechanisms of primary chemoresistance in ovarian carcinomas. *Clinical cancer research : an official journal of the American Association for Cancer Research* **15**, 1417-1427, doi:10.1158/1078-0432.CCR-08-1564 (2009).
21 Nakayama, N. *et al.* Gene amplification CCNE1 is related to poor survival and potential therapeutic target in ovarian cancer. *Cancer* **116**, 2621-2634, doi:10.1002/cncr.24987 (2010).
22 Aziz, D. *et al.* 19q12 amplified and non-amplified subsets of high grade serous ovarian cancer with overexpression of cyclin E1 differ in their molecular drivers and clinical outcomes. *Gynecologic oncology* **151**, 327-336, doi:10.1016/j.ygyno.2018.08.039 (2018).
23 Domcke, S., Sinha, R., Levine, D. A., Sander, C. & Schultz, N. Evaluating cell lines as tumour models by comparison of genomic profiles. *Nature communications* **4**, 2126, doi:10.1038/ncomms3126 (2013).
24 Anglesio, M. S. *et al.* Type-specific cell line models for type-specific ovarian cancer research. *PloS one* **8**, e72162, doi:10.1371/journal.pone.0072162 (2013).
25 Papp, E. *et al.* Integrated Genomic, Epigenomic, and Expression Analyses of Ovarian Cancer Cell Lines. *Cell reports* **25**, 2617-2633, doi:10.1016/j.celrep.2018.10.096 (2018).
26 Petermann, E., Orta, M. L., Issaeva, N., Schultz, N. & Helleday, T. Hydroxyurea-stalled replication forks become progressively inactivated and require two different RAD51-mediated pathways for restart and repair. *Molecular cell* **37**, 492-502, doi:10.1016/j.molcel.2010.01.021 (2010).
27 Marteil, G. *et al.* Over-elongation of centrioles in cancer promotes centriole amplification and chromosome missegregation. *Nature communications* **9**, 1258, doi:10.1038/s41467-018-03641-x (2018).

28 Milagre, C. S. *et al.* Adaptive Upregulation of EGFR Limits Attenuation of Tumor Growth by Neutralizing IL6 Antibodies, with Implications for Combined Therapy in Ovarian Cancer. *Cancer research* **75**, 1255-1264, doi:10.1158/0008-5472.CAN-14-1801 (2015).
29 Merritt, M. A. *et al.* Gene expression signature of normal cell-of-origin predicts ovarian tumor outcomes. *PloS one* **8**, e80314, doi:10.1371/journal.pone.0080314 (2013).
30 Labidi-Galy, S. I. *et al.* High grade serous ovarian carcinomas originate in the fallopian tube. *Nature communications* **8**, 1093, doi:10.1038/s41467-017-00962-1 (2017).
31 Scheinin, I. *et al.* DNA copy number analysis of fresh and formalin-fixed specimens by shallow whole-genome sequencing with identification and exclusion of problematic regions in the genome assembly. *Genome research* **24**, 2022-2032, doi:10.1101/gr.175141.114 (2014).
32 Worrall, J. T. *et al.* Non-random Mis-segregation of Human Chromosomes. *Cell reports* **23**, 3366-3380, doi:10.1016/j.celrep.2018.05.047 (2018).
33 Manning, A. L., Longworth, M. S. & Dyson, N. J. Loss of pRB causes centromere dysfunction and chromosomal instability. *Genes & development* **24**, 1364-1376, doi:10.1101/gad.1917310 (2010).
34 Ganem, N. J., Godinho, S. A. & Pellman, D. A mechanism linking extra centrosomes to chromosomal instability. *Nature* **460**, 278-282, doi:10.1038/nature08136 (2009).
35 Kwon, M. *et al.* Mechanisms to suppress multipolar divisions in cancer cells with extra centrosomes. *Genes & development* **22**, 2189-2203, doi:10.1101/gad.1700908 (2008).
36 Silkworth, W. T., Nardi, I. K., Scholl, L. M. & Cimini, D. Multipolar spindle pole coalescence is a major source of kinetochore mis-attachment and chromosome mis-segregation in cancer cells. *PloS one* **4**, e6564, doi:10.1371/journal.pone.0006564 (2009).
37 Luddecke, S. *et al.* The putative oncogene CEP72 inhibits the mitotic function of BRCA1 and induces chromosomal instability. *Oncogene*, doi:10.1038/onc.2015.290 (2015).
38 Stolz, A., Ertych, N. & Bastians, H. A phenotypic screen identifies microtubule plus end assembly regulators that can function in mitotic spindle orientation. *Cell Cycle* **14**, 827-837, doi:10.1080/15384101.2014.1000693 (2015).
39 Bartkova, J. *et al.* Replication stress and oxidative damage contribute to aberrant constitutive activation of DNA damage signalling in human gliomas. *Oncogene* **29**, 5095-5102, doi:10.1038/onc.2010.249 (2010).
40 Bartkova, J. *et al.* ATM activation in normal human tissues and testicular cancer. *Cell Cycle* **4**, 838-845 (2005).
41 Pathania, S. *et al.* BRCA1 haploinsufficiency for replication stress suppression in primary cells. *Nature communications* **5**, 5496, doi:10.1038/ncomms6496 (2014).
42 Mijic, S. *et al.* Replication fork reversal triggers fork degradation in BRCA2-defective cells. *Nature communications* **8**, 859, doi:10.1038/s41467-017-01164-5 (2017).
43 Schlacher, K. *et al.* Double-strand break repair-independent role for BRCA2 in blocking stalled replication fork degradation by MRE11. *Cell* **145**, 529-542, doi:10.1016/j.cell.2011.03.041 (2011).

44 Lukas, C. *et al.* 53BP1 nuclear bodies form around DNA lesions generated by mitotic transmission of chromosomes under replication stress. *Nature cell biology* **13**, 243-253, doi:10.1038/ncb2201 (2011).
45 Bester, A. C. *et al.* Nucleotide deficiency promotes genomic instability in early stages of cancer development. *Cell* **145**, 435-446, doi:10.1016/j.cell.2011.03.044 (2011).
46 N. Shaikh, A. M., B. Bakker, D. Muliaditan, D.C.J. Spierings, F. Foijer, S.E. McClelland. Replication stress generates multiple distinct classes of DNA copy number alteration. *BioRXiv* **doi.org/10.1101/743658** (2019).
47 Zheng, F. *et al.* Mechanism and current progress of Poly ADP-ribose polymerase (PARP) inhibitors in the treatment of ovarian cancer. *Biomed Pharmacother* **123**, 109661, doi:10.1016/j.biopha.2019.109661 (2020).
48 Bee, L., Fabris, S., Cherubini, R., Mognato, M. & Celotti, L. The efficiency of homologous recombination and non-homologous end joining systems in repairing double-strand breaks during cell cycle progression. *PloS one* **8**, e69061, doi:10.1371/journal.pone.0069061 (2013).
49 Liu, N. XRCC2 is Required for the Formation of Rad51 Foci Induced by Ionizing Radiation and DNA Cross-Linking Agent Mitomycin C. *J Biomed Biotechnol* **2**, 106-113, doi:10.1155/S1110724302204040 (2002).
50 Piccart, M. J. *et al.* Randomized intergroup trial of cisplatin-paclitaxel versus cisplatin-cyclophosphamide in women with advanced epithelial ovarian cancer: three-year results. *Journal of the National Cancer Institute* **92**, 699-708 (2000).
51 Lee, S. B. *et al.* Tousled-like kinases stabilize replication forks and show synthetic lethality with checkpoint and PARP inhibitors. *Sci Adv* **4**, eaat4985, doi:10.1126/sciadv.aat4985 (2018).
52 Bielski, C. M. *et al.* Genome doubling shapes the evolution and prognosis of advanced cancers. *Nature genetics* **50**, 1189-1195, doi:10.1038/s41588-018-0165-1 (2018).
53 Wilhelm, T. *et al.* Spontaneous slow replication fork progression elicits mitosis alterations in homologous recombination-deficient mammalian cells. *Proceedings of the National Academy of Sciences of the United States of America* **111**, 763-768, doi:10.1073/pnas.1311520111 (2014).
54 Shang, Z. *et al.* DNA-PKcs activates the Chk2-Brca1 pathway during mitosis to ensure chromosomal stability. *Oncogenesis* **3**, e85, doi:10.1038/oncsis.2013.49 (2014).
55 Godinho, S. A. *et al.* Oncogene-like induction of cellular invasion from centrosome amplification. *Nature* **510**, 167-171, doi:10.1038/nature13277 (2014).
56 Bohly, N., Kistner, M. & Bastians, H. Mild replication stress causes aneuploidy by deregulating microtubule dynamics in mitosis. *Cell Cycle* **18**, 2770-2783, doi:10.1080/15384101.2019.1658477 (2019).
57 Orr, B. & Compton, D. A. A double-edged sword: how oncogenes and tumor suppressor genes can contribute to chromosomal instability. *Front Oncol* **3**, 164, doi:10.3389/fonc.2013.00164 (2013).
58 Kotsantis, P., Petermann, E. & Boulton, S. J. Mechanisms of Oncogene-Induced Replication Stress: Jigsaw Falling into Place. *Cancer discovery* **8**, 537-555, doi:10.1158/2159-8290.CD-17-1461 (2018).
59 Teixeira, L. K. *et al.* Cyclin E Deregulation Promotes Loss of Specific Genomic Regions. *Current Biology* **25**, 1327-1333, doi:10.1016/j.cub.2015.03.022 (2015).

60 Ruiz, S. *et al.* Limiting replication stress during somatic cell reprogramming reduces genomic instability in induced pluripotent stem cells. *Nature communications* **6**, 8036, doi:10.1038/ncomms9036 (2015).
61 Halliwell, J. A. *et al.* Nucleosides Rescue Replication-Mediated Genome Instability of Human Pluripotent Stem Cells. *Stem cell reports* **14**, 1009-1017, doi:10.1016/j.stemcr.2020.04.004 (2020).
62 Chaudhuri, A. R. *et al.* Replication fork stability confers chemoresistance in BRCA-deficient cells. *Nature*, 1-25, doi:10.1038/nature18325 (2016).
63 Sullivan-Reed, K. *et al.* Simultaneous Targeting of PARP1 and RAD52 Triggers Dual Synthetic Lethality in BRCA-Deficient Tumor Cells. *Cell reports* **23**, 3127-3136, doi:10.1016/j.celrep.2018.05.034 (2018).
64 Orre, L. M. *et al.* p53 is involved in clearance of ionizing radiation-induced RAD51 foci in a human colon cancer cell line. *Biochemical and biophysical research communications* **342**, 1211-1217, doi:10.1016/j.bbrc.2006.02.085 (2006).
65 Murnyak, B. & Hortobagyi, T. Immunohistochemical correlates of TP53 somatic mutations in cancer. *Oncotarget* **7**, 64910-64920, doi:10.18632/oncotarget.11912 (2016).

Figure legends

Figure 1: HGSC cell lines display numerical and structural chromosome defects and persistent chromosome segregation errors. **A)** DNA copy number profiles computed from whole genome sequencing data for HGSC cell lines. **B)** Representative image of a metaphase spread from Ovsaho. Pan-centromere FISH staining indicated in green (panCEN); scale bar 10 μm. **C)** Ploidy of each cell line was derived from metaphase spread analysis. For each cell line, twenty metaphase spreads were analysed across two experiments. **D)** M-FISH analysis of metaphase spreads showing structural and numerical aberrations from FNE1 and Kuramochi. **E)** Stills taken from movies of Ovsaho cells stably expressing H2B-RFP (white). Time in minutes is indicated post nuclear envelope breakdown (NEBD). Arrowhead indicates chromatin bridge. **F)** Chromosome segregation error rates from live cell movies. Data shown is from two independent experiments. **G)** Immunofluorescence images of anaphase cells probed with antibodies to CREST (red, marks centromere) and Hec1 (green, marks kinetochore) exhibiting

different classes of segregation errors; lagging centric, lagging acentric, anaphase bridge. **H)** Analysis of segregation errors of all cell lines from immunofluorescence images, from four to seven experiments (179-300 anaphase cells per cell line). **I)** Anaphase cells with errors from H were classified according to error type (either centric, acentric or bridge errors or a mixture of any or all three types). **J)** Cov318 anaphase cells with multiple errors, and error types, per cell. **K,L)** FISH with centromeric probes (PanCEN; green) was used to define whether lagging chromatin (red) was positive (centric) or negative (acentric) for DNA centromere sequence, quantified in (L) for 108 anaphases in G33 cell line.

Figure 2: HGSC cell lines prolong mitosis due to slow alignment of chromosomes to the metaphase plate; low dose paclitaxel can reduce MT dynamics and CIN. A) Stills from movies of cell lines stably expressing H2B-RFP (white). Time in minutes is indicated post nuclear envelope breakdown (NEBD). Frames where the last chromosome completed congression to the metaphase plate (LCC) and where anaphase onset (AO) began, are indicated. Scale bar represents 5 μm. **B)** Time taken for cells to progress from NEBD to anaphase onset. Each circle represents timing for one cell. Data taken from two independent experiments; 22-126 cells analysed per cell line in total. Statistical difference between HGSC cancer cell lines and FNE1 control is indicated (one-way ANOVA with Dunnett's correction for multiple testing). **C)** Time taken for cells to progress from NEBD to last chromosome congressed (LCC) to the metaphase plate. Data taken from two independent experiments. 26-109 cells analysed per cell line in total. Statistical test as in (B). Differences between HGSC cancer cell lines compared to FNE1 are shown. **D)** Length of time cells remained arrested in mitosis after treatment with nocodazole**,** to assess Spindle Assembly Checkpoint**.** Summary of one (Snu119, FNE1), two (Cov318, Kuramochi) or three (G164) experiments. **E)** Stills from live movies of cells expressing EB3-GFP, arrested in mitosis using monastrol. **F)** Analysis of microtubule dynamics from EB3-GFP live imaging tip tracking assay. Statistical test performed as in (B). **G)** Prometaphase cells arrested with monastrol, showing normal symmetric (HCT116) or abnormal asymmetric (Cov318) spindle morphology. **H)** Quantification of abnormal spindle morphology in cells arrested with monastrol in conjunction with 0, 1 or 2 nM paclitaxel. **I)** Microtubule assembly rates in cells expressing EB3-GFP, arrested with monastrol and treated with either DMSO or 1 nM paclitaxel. **J, K)** Segregation error rates of cells after 2 hr treatment with DMSO or 1 nM paclitaxel. T-tests were performed in I) and K) between pairs as indicated. Scale bars 5

(in A) or 10 μm (in G). Asterisks denote significance (*p<0.05, **p<0.01, ***p<0.001 ****p<0.0001, or non-significant (p>0.05; ns)).

Figure 3: HGSC cell lines exhibit replication stress that contributes to chromosome mis-segregation and CIN. A) Histograms for replication fork rates as measured by DNA fibre assays (99-202 fibres analysed in total for each cell line; examples of fibres shown on right, with average calculated speed). CIN-positive SW620 and CIN-negative HCT116 colorectal cancer cell lines were used as controls for slow, and normal replication fork rates respectively. **B)** Example immunofluorescence (IF) image of prometaphase cell stained for γH2AX. Quantification given below image. **C)** Example of IF image of a G1 (Cyclin A negative) cell stained for 53BP1 bodies, with quantification. **D)** Example IF image of an anaphase cell with an ultrafine bridge as demonstrated by a DAPI-negative, RPA bridge, with quantification. Statistical tests for (b-d) are one-way ANOVA with Dunnett's correction for multiple testing using FNE1 as control. **E, F)** Segregation error rates of cells treated with nucleosides, given as fold change of errors in untreated cells (see **Figure S4** for raw data). Significance from t-test for each treated/untreated pair is indicated. **G)** Examples of clonal FISH images, with cells stained for probes against centromere enumeration probes (CEP) of chromosomes 3 (CEP3; red) and 6 (CEP6; green). **H)** Analysis of numerical CIN using clonal FISH without or with nucleoside treatment. For each cell line, each circle indicates percentage of cells in a colony deviating from modal value (modes given below graph) of that chromosome in that colony. T-test between pairs is shown. **I, J)** 53BP1 bodies in Cyclin A-negative (G1) cells were quantified in cells treated for 24 hr with DMSO or aphidicolin (0.2 μM). Summary of two experiments, n=65-187 cells. Asterisks denote significance (*p<0.05, **p<0.01, ***p<0.001 ***p<0.0001, or non-significant (ns)). Green bars in B,C,D,H,J indicate mean. Scale bars represent 5 μm in all images, except 20 μm in (G).

Figure 4: HGSC response to chemotherapy. A) Proliferation dose response to PARPi. Dotted line indicates where proliferation dropped below 50% of DMSO treated cells. Mean and standard deviation from three independent experiments is shown. **B)** FNE1 cells (untreated or 2 hr recovery after irradiation with 2 Gy) stained for Rad51 and Cyclin A. Scale bar represents 5 μm. **C)** Quantification of Rad51 foci in S/G2 cells (Cyclin A positive) in untreated cells or in cells with 2 hr or 24 hr recovery from irradiation with 2 Gy. Red line indicates mean from three independent experiments. **D)** Proliferation dose response to paclitaxel. Dotted line indicates

where proliferation dropped below 50% of DMSO treated. Mean and standard deviation from three independent experiments (one for Ovkate). **E**) Correlation between microtubule assembly rates (from **Figure 2f**) and paclitaxel resistance (approximate value for paclitaxel dose causing proliferation to drop to 50% of DMSO controls, as a log scale, taken from **Figure 4d**) in HGSC cell lines. Pearson's correlation with p-value indicated.

Figure 5 (relating to Discussion): Phenotype summary. (A) Clustering of HGSC cell lines according to extent of their functional CIN phenotypes. **(B)** Relationships between different CIN phenotypes in this study; Pearson's Correlation and p-value given for each.

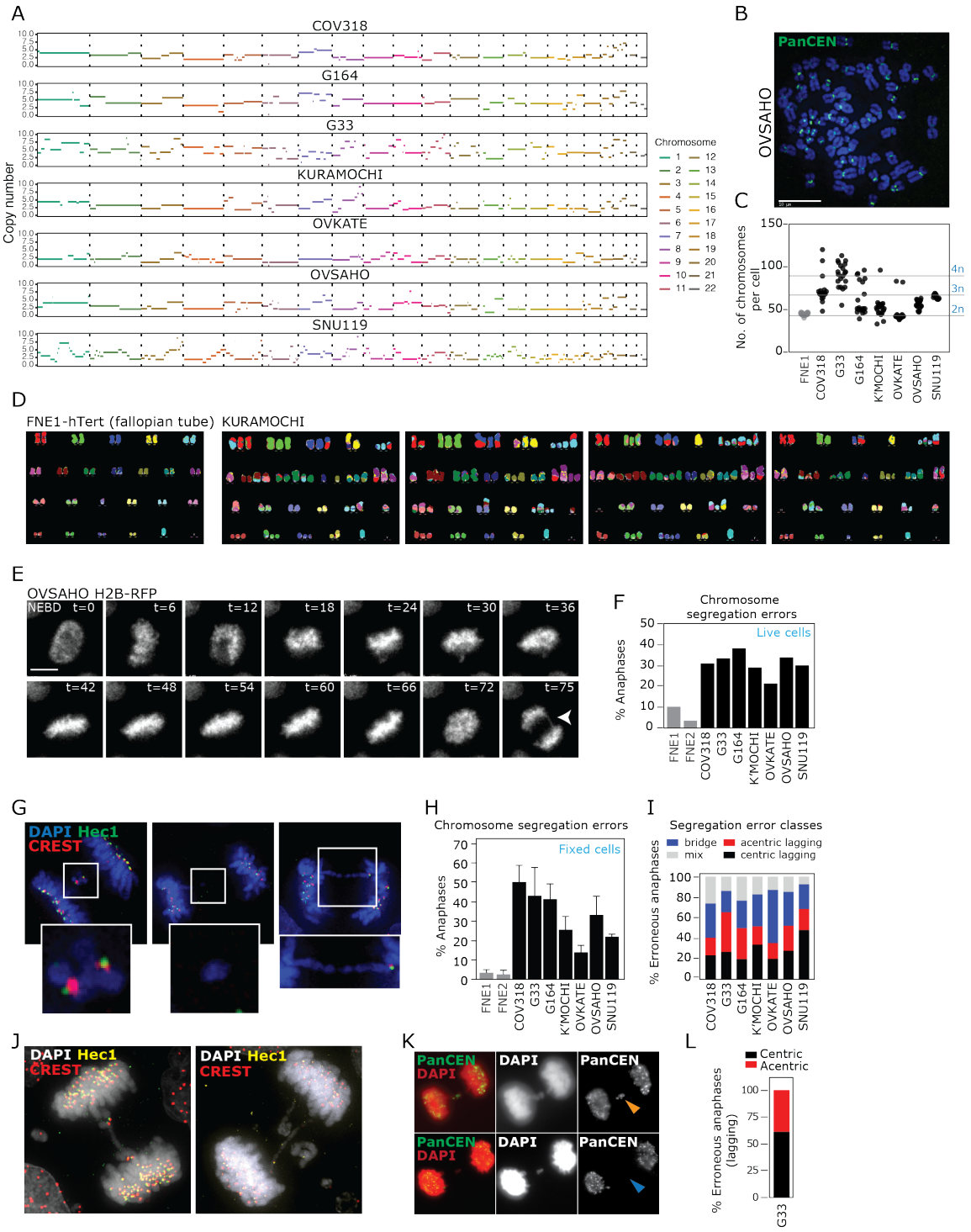
A
COV318
G164
G33
KURAMOCHI
OVKATE
OVSAHO
SNU119
Copy number
Chromosome
B
PanCEN
OVSAHO
C
No. of chromosomes per cell
4n
3n
2n
FNE1
COV318
G33
G164
K'MOCHI
OVKATE
OVSAHO
SNU119
D
FNE1-hTert (fallopian tube)
KURAMOCHI
E
OVSAHO H2B-RFP
NEBD t=0
t=6
t=12
t=18
t=24
t=30
t=36
t=42
t=48
t=54
t=60
t=66
t=72
t=75
F
Chromosome segregation errors
Live cells
% Anaphases
G
DAPI Hec1
CREST
H
Chromosome segregation errors
Fixed cells
% Anaphases
I
Segregation error classes
bridge
mix
acentric lagging
centric lagging
% Erroneous anaphases
J
DAPI Hec1
CREST
K
PanCEN
DAPI
L
Centric
Acentric
% Erroneous anaphases (lagging)

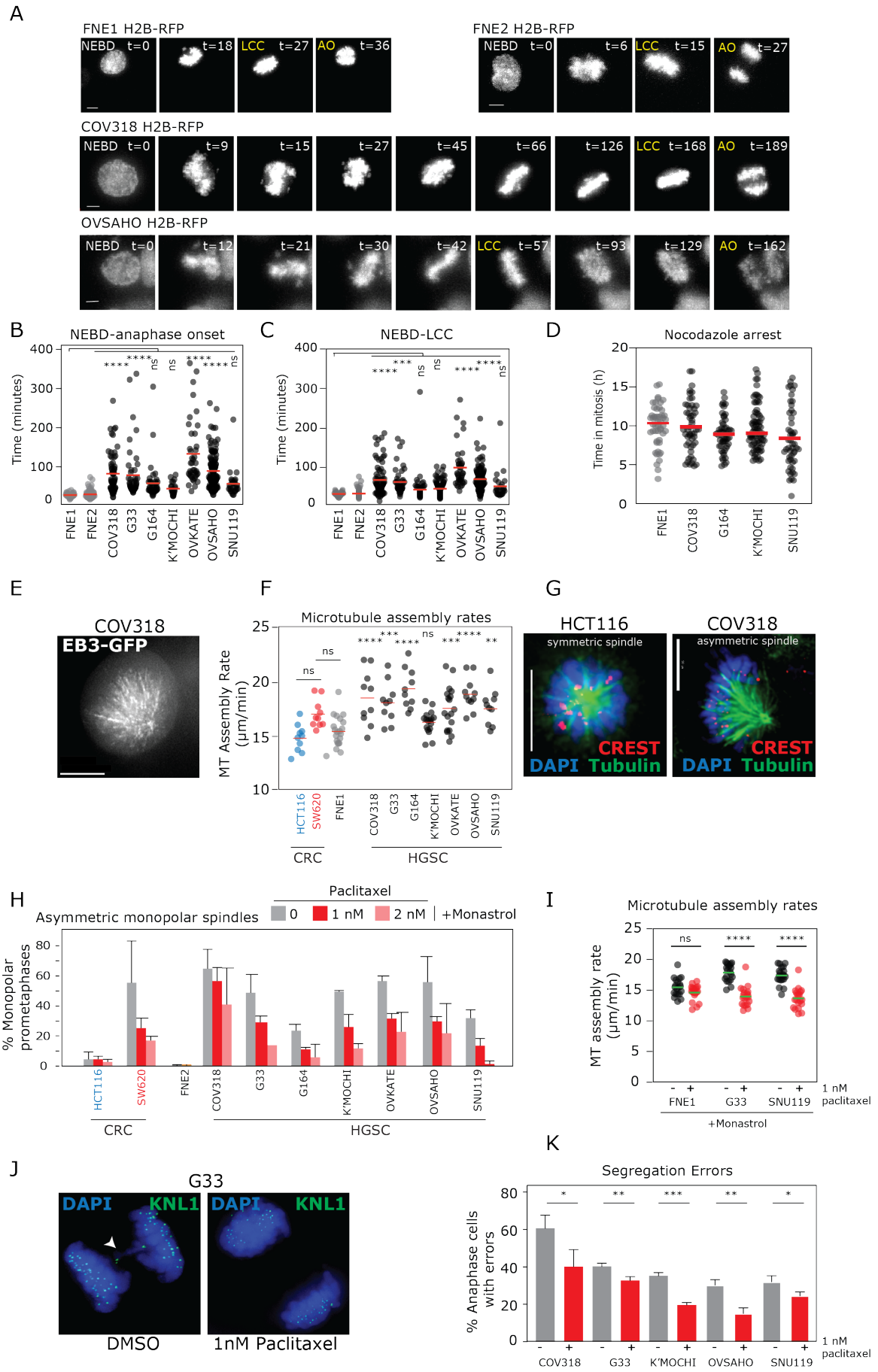
A
FNE1 H2B-RFP
NEBD t=0
t=18
LCC t=27
AO t=36
FNE2 H2B-RFP
NEBD t=0
t=6
LCC t=15
AO t=27
COV318 H2B-RFP
NEBD t=0
t=9
t=15
t=27
t=45
t=66
t=126
LCC t=168
AO t=189
OVSAHO H2B-RFP
NEBD t=0
t=12
t=21
t=30
t=42
LCC t=57
t=93
t=129
AO t=162
B
NEBD-anaphase onset
Time (minutes)
FNE1
FNE2
COV318
G33
G164
K'MOCHI
OVKATE
OVSAHO
SNU119
C
NEBD-LCC
Time (minutes)
D
Nocodazole arrest
Time in mitosis (h)
E
COV318
EB3-GFP
F
Microtubule assembly rates
MT Assembly Rate (µm/min)
HCT116
SW620
CRC
HGSC
G
HCT116
symmetric spindle
COV318
asymmetric spindle
CREST
DAPI Tubulin
H
Paclitaxel
Asymmetric monopolar spindles
0
1 nM
2 nM
+Monastrol
% Monopolar prometaphases
I
Microtubule assembly rates
MT assembly rate (µm/min)
1 nM paclitaxel
+Monastrol
J
G33
DAPI KNL1
DMSO
1nM Paclitaxel
K
Segregation Errors
% Anaphase cells with errors
1 nM paclitaxel

Tamura et al Paper 1 FIGURE 3

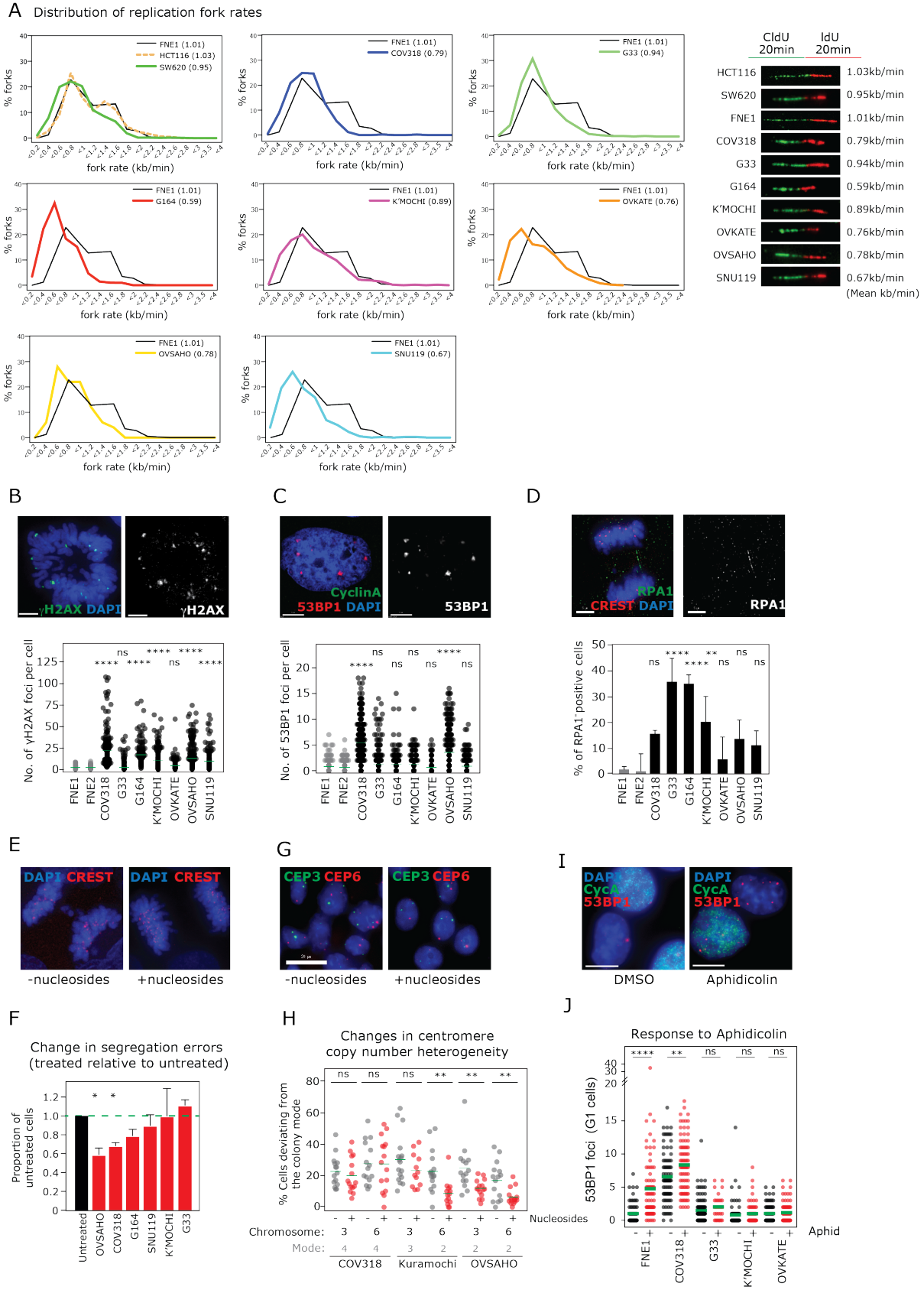

Tamura et al Paper 1 FIGURE 4

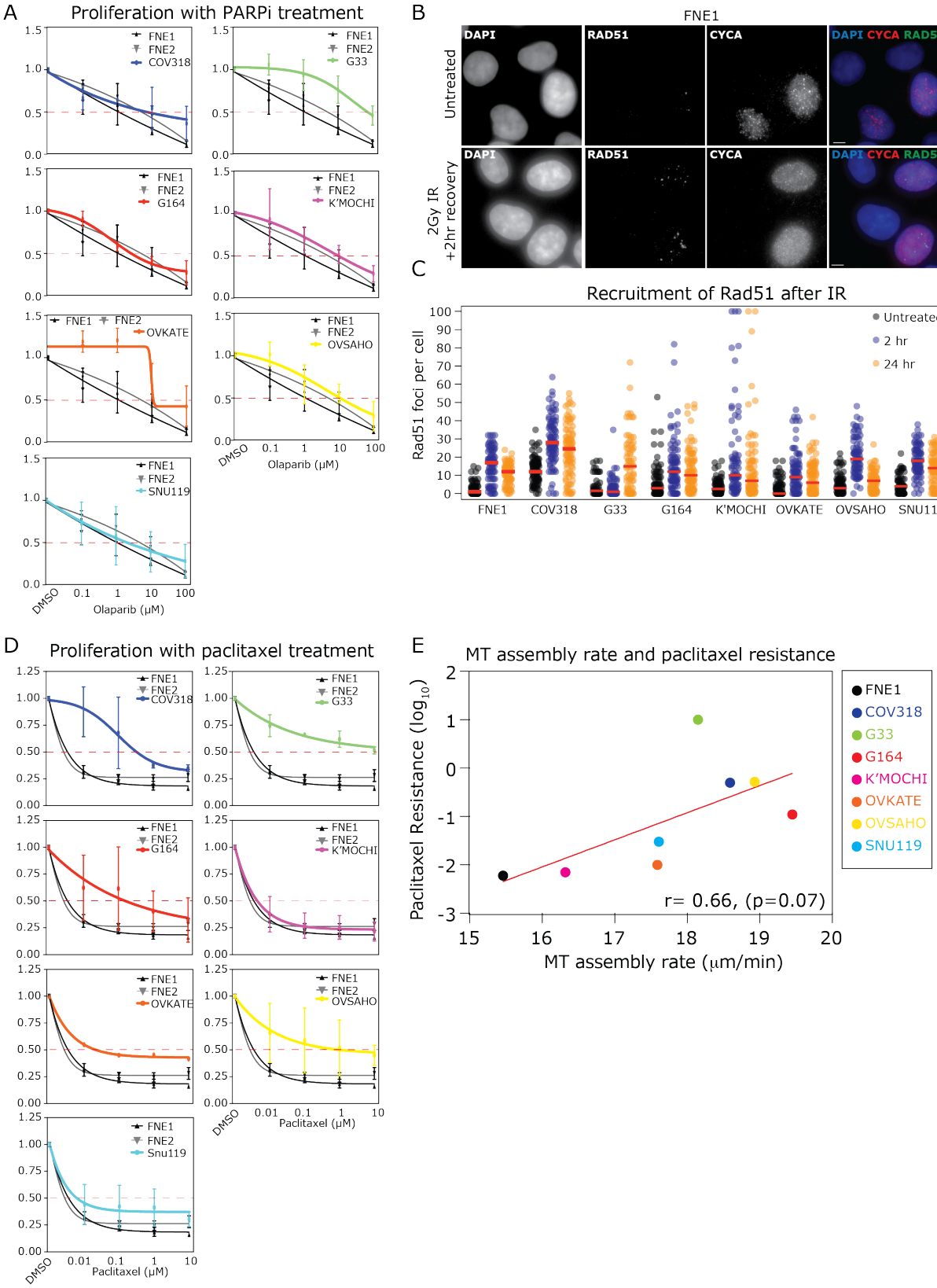

Tamura et al Paper 1 FIGURE 5